ACS APPLIED MATERIALS & INTERFACES

Research Article

Cite This: ACS Appl. Mater. Interfaces 2019, 11, 28154−28163

www.acsami.org

# Highly Sensitive $As^{3+}$ Detection Using Electrodeposited Nanostructured $MnO_x$ and Phase Evolution of the Active Material during Sensing

Tanvi Gupte,[†,‡,§] Sourav Kanti Jana,[†,§] Jyoti Sarita Mohanty,[†] Pillalamarri Srikrishnarka,[†] Sritama Mukherjee,[†] Tripti Ahuja,[†] Chennu Sudhakar,[†] Tiju Thomas,*[,‡] and Thalappil Pradeep*[,†]

[†]DST Unit of Nanoscience (DST UNS) and Thematic Unit of Excellence, Department of Chemistry and [‡]Department of Metallurgical and Materials Engineering, Indian Institute of Technology Madras, Chennai 600036, India

Supporting Information

**ABSTRACT:** A simple, one-step electrodeposition approach has been used to fabricate $MnO_x$ on an indium-doped tin oxide substrate for highly sensitive $As^{3+}$ detection. We report an experimental limit of detection of 1 ppb through anodic stripping voltammetry with selectivity to $As^{3+}$ in the presence of 10 times higher concentrations of several metal ions. Additionally, we report the simultaneous phase evolution of active material occurring through multiple stripping cycles, wherein $MnO/Mn_2O_3$ eventually converts to $Mn_3O_4$ as a result of change in the oxidation states of manganese. This occurs with concomitant changes in morphology. Change in the electronic property (increased charge transfer resistance) of the material due to sensing results in an eventual decrease in sensitivity after multiple stripping cycles. In a nutshell, this paper reports stripping-voltammetry-induced change in morphology and phase of as-prepared Mn-based electrodes during As sensing.

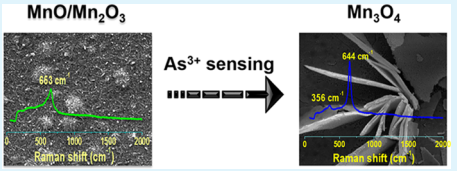


**KEYWORDS:** *arsenic, nanostructured electrode, manganese oxide, electrochemical sensor, stripping voltammetry*

## 1. INTRODUCTION

Arsenic (As) contamination in water is a serious concern, affecting over 140 million people worldwide.[1] Arsenic mainly exists as arsenate [As(V)] and arsenite [As(III)] ions in water and soil.[2] Currently, the World Health Organization (WHO) and U.S. Environmental Protection Agency recommended that the limit of arsenic content in drinking water is 10 $\mu$g/L (or 10 parts per billion (ppb)).[3,4] Use of As-contaminated water for the preparation of food, irrigation of crops, and drinking has serious consequences on human health.[3] Most known As and inorganic As compounds are classified as Group 1 human carcinogens by International Agency for Research on Cancer.[5] Group 1 compounds are those for which there is sufficient evidence for concluding their carcinogenicity in humans. Prolonged exposure to high concentrations of arsenic may cause cancer of skin, lungs, kidney, uterus, and liver. It can also lead to disorders of cardiovascular, gastrointestinal, and central nervous systems.[6] The trivalent arsenic ($As^{3+}$) has higher mobility in groundwater and is more toxic than the pentavalent ($As^{5+}$) analogue.[7]

Therefore, accurate and selective detection of $As^{3+}$ in water is more important to identify the contaminated source, to help prevent its deleterious effects on health, and also to optimize arsenic remediation technologies. Various laboratory-based arsenic detection techniques have been used such as hydride generation/atomic absorption spectrometry, graphite furnace atomic absorption spectrometry, inductively coupled plasma-mass spectrometry (ICP-MS), atomic fluorescence spectrometry, etc.[2,8,9] However, such techniques are expensive, unsuitable for on-field testing, and often require prior separation of arsenic species (speciation). Thus, there is a demand for an affordable arsenic sensor, especially because most of the arsenic-affected people are poor. Electrochemical sensors offer a low-cost, rapid, portable, reliable, and sensitive method. For the detection of arsenic, both enzymatic[10−12] and non-enzymatic[13−16] electrochemical sensors have been developed. Non-enzymatic sensors are important as they can offer stability and cost-effectiveness and support diverse operating conditions.

On the other hand, enzyme-based biosensors have an advantage due to their analyte specificity and lower limits of detection. However, they have certain intrinsic limitations such as complicated enzyme immobilization procedures, limited lifetime, instability at various pH and temperature conditions, and expensive preparation and storage conditions.[17−20] Therefore, tailoring of non-enzymatic electrode surfaces is desirable for $As^{3+}$ sensing with good sensitivity and stability.

Anodic stripping voltammetry (ASV) has been used widely for quantitative measurement of arsenic in water.[13,14,21,15] It is an ultrasensitive, two-step voltammetric technique for quantitative determination of specific ionic species. The first step is the deposition or preconcentration step in which the analyte of interest is usually electrodeposited on the working electrode at a constant potential for a certain time. This step

Received: April 6, 2019
Accepted: July 12, 2019
Published: July 12, 2019






DOI: 10.1021/acsami.9b06023
ACS Appl. Mater. Interfaces 2019, 11, 28154−28163

involves reduction of the metal ions from the solution to the electrode surface (for example, $As^{3+}$ to $As^0$). In the second step, the potential of the working electrode is raised to a higher value by applying a voltage scan (termed as anodic stripping). At a definite potential, specific metal species which are deposited onto the electrode surface are stripped (oxidized) into the solution (for example, $As^0$ to $As^{3+}$). The oxidation of analyte (arsenic in this case) is recorded as a peak in terms of Faradaic oxidation current in the voltammogram at a particular potential called the oxidation potential of the arsenic species. The peak intensity is proportional to the $As^{3+}$ concentration present in the electrolyte.[17] In our study, linear sweep stripping voltammetry (LSSV), a type of ASV technique, has been used for $As^{3+}$ detection, wherein the potential is swept linearly with time.

In this work, a transition metal oxide (TMO) (manganese oxide ($MnO_x$))-based working electrode was developed and used as an electrochemical sensor to detect $As^{3+}$ present in water. TMO adsorbents are considered as some of the promising materials for removal of toxic heavy metal ions from high-total dissolved solid groundwater because of their abundant physicochemical properties such as large surface area, specific adsorption sites, and catalytic activity.[4] These properties are mainly affected by the electronic properties and surface morphology of the TMO. Manganese oxides exist as $MnO_6$ octahedra that form tunnels and/or layered structures.[22,23] The tunnels and layers are connected by corner or edge sharing. Cations and water molecules can occupy these tunnels or interlayers.[24] The nanostructured $MnO_x$ provides active sites for arsenic adsorption during sensing. Sorption of As on manganese oxide ($MnO_x$)-based materials due to their selective adsorption property is widely reported.[25−27] Mn oxides are known to be one of the strongest naturally occurring oxidizing agents.[24] Also, the surface areas of different oxides of manganese may vary from 3 to ∼200 $m^2/g$.[28] These properties of $MnO_x$ influence the biogeochemical cycling of contaminants, such as chromium (Cr), uranium (U), selenium (Se), and arsenic.[24] Several electrochemical As sensors have been developed to utilize these properties of $MnO_x$. Many of them use working electrodes of $MnO_x$ modified with gold nanoparticles,[15,29] reduced graphene oxide,[13] etc. for better sensitivity and selectivity. Here, we would like to mention that this study deals with two aspects: one is electrochemically developing a nanostructured $MnO_x$-based electrode for $As^{3+}$ sensing. The second aspect is a detailed insight into the fundamental, yet unexplored, issue of phase evolution and morphological changes in the nanosystem during electrochemical sensing. Manganese oxides exist in several oxidation states. The stripping-voltammetry-induced changes in nanostructures and oxidation states are studied in this paper by performing several characterization studies before and after sensing. As of now, a few $MnO_x$-based composite nanostructures have been reported for $As^{3+}$ sensing.[13,29,30] However, reports are scarce about the impact of voltammetric techniques on the active material and it is important to understand the phase and structural stability of the material during the process of sensing. This is a crucial contributing factor for limiting the performance of such sensors in the course of their operation.

Here, we have used a noble-metal-free working electrode, wherein $MnO_x$ was electrodeposited on an indium-doped tin oxide (ITO)-coated glass substrate for As detection. Various working electrode substrates have been used for As detection, e.g., platinum,[31] gold,[14,18,31] glassy carbon,[13,15,29] boron-doped diamond,[16,32] etc. Although these materials are promising, there are often disadvantages associated with their use such as high cost, need of strongly acidic media for operation (which can produce toxic arsine gas), chemical modification with an electron transfer mediator, etc. ITO as an electrode substrate is of great interest in electrochemical sensors because of low cost and good electrical conductivity (∼$10^4$ S/cm).[33] We have studied the electrochemistry-induced evolution of phase and morphology of $MnO_x$ and its impact on the electronic conductivity and electrochemical property of the electrodeposited material.

The phase and morphology of $MnO_x$ were controlled through electrodeposition by the cyclic voltammetry (CV) technique performed at three different potential windows. The electrodes were characterized by electron microscopy, spectroscopy, and electrochemical techniques. LSSV was performed using different concentrations of $As^{3+}$. Quantitative detection of $As^{3+}$ with a linear response range from 1 to 150 ppb was observed using an optimized $MnO_x$/ITO electrode. The $As^{3+}$ response was saturated at ∼125−150 ppb after multiple stripping cycles. The phase evolution of active material wherein $MnO/Mn_2O_3$ eventually got converted to $Mn_3O_4$ resulted in an increase in the charge transfer resistance of the material, which was studied by impedance spectroscopy. This may be the reason for eventual decrease in sensitivity after multiple stripping cycles. Moreover, selectivity of the electrode for $As^{3+}$ was successfully studied in the presence of 10 times higher concentrations of several metal ions.

## 2. EXPERIMENTAL SECTION

**2.1. Materials.** Anhydrous manganese acetate [$Mn(CH_3COO)_2$], sodium sulfate ($Na_2SO_4$), sodium arsenite ($NaAsO_2$), ITO-coated glass substrates, and Millipore-produced deionized (DI) water (∼18.2 MΩ) were used throughout the experiments.

**2.2. Preparation of Working Electrode by Electrodeposition.** ITO-coated glass substrates were cleaned by ultrasonicating them sequentially in acetone, ethanol, and distilled water for 5 min each, followed by drying in nitrogen. The working electrode was prepared by electrodeposition of manganese oxide on the cleaned ITO substrate (∼1 $cm^2$), and this as-prepared electrode is termed $MnO_x$/ITO. The geometric surface area of ITO was maintained by sticking a strip of scotch tape as a mask on the substrate. A three-electrode setup comprising ITO as the working electrode, platinum wire as a counter electrode, and Ag/AgCl as a reference electrode was used during electrochemical measurements. An aqueous solution of 0.05 M $Mn(CH_3COO)_2$ was used as a precursor, and 0.1 M sodium sulfate ($Na_2SO_4$) was used as electrolyte during electrochemical deposition of $MnO_x$. Electrodeposition was carried out by CV at three different potential ranges: 0.8−1.3 V (8 cycles), −0.2−0.9 V (15 cycles), and −1−1.3 V (4 cycles) at a scan rate of 0.05 V/s using a CHI 600A electrochemical workstation at room temperature. Subsequently, these samples were named **M1**, **M2**, and **M3**, respectively, and the same will be used further in this paper. The electrodeposition potential ranges were set based on the Pourbaix diagram of manganese (Figure S1).[34] After electrodeposition, the samples were washed in distilled water, dried in air, and finally stored at room temperature before using for further material characterization and electrochemical analysis.

**2.3. Electrochemical Analysis.** Arsenic sensing was carried out by the linear sweep stripping voltammetry (LSSV) technique using $NaAsO_2$ dissolved in phosphate-buffered saline (PBS, pH ∼ 7.4) with the following optimized parameters: deposition potential (DP) of $As^{3+}$ of −0.7 V, deposition time (DT) of 180 s, stripping potential range of −0.40−0.20 V, and scan rate of 0.05 V/s. All of the electrochemical measurements were performed using $MnO_x$/ITO, Pt wire, and Ag/AgCl as working, counter, and reference electrodes,


DOI: 10.1021/acsami.9b06023
ACS Appl. Mater. Interfaces 2019, 11, 28154−28163

respectively. For arsenite sensing, different concentrations of $As^{3+}$ were prepared in PBS just before recording LSSV. The electrodes were washed with DI water between consecutive measurements. CV measurements for testing the performance of bare ITO at optimized parameters were performed using bare ITO as the working electrode. Counter and reference electrodes were the same as above. The redox molecule used was 32.6 $\mu$M potassium ferricyanide ($K_3Fe(CN)_6$) in 3.2 mM potassium chloride (KCl) as the supporting electrolyte. The volume of electrolyte was maintained constant for all of the electrochemical measurements.

**2.4. Instrumentation.** All electrochemical measurements including electrodeposition and LSSV for $As^{3+}$ detection were performed using a CH 600A (CH Instruments) electrochemical workstation. Surface morphology of $MnO_x$ samples was obtained using a MIRA 3 (TESCAN) field emission scanning electron microscope (FESEM). All high-resolution transmission electron microscopy (HRTEM) images were obtained using JEOL JFD 3010 (JEOL Japan), a 300 kV transmission electron microscope, equipped with an ultra-high-resolution pole piece. X-ray diffraction (XRD) patterns of $MnO_x$ were obtained with Bruker X8 KAPPA using Cu K$\alpha$ radiation as the source. Electrochemical impedance spectroscopy (EIS) measurements were performed using a Biologic electrochemical analyser (SP200). Inductively coupled plasma-mass spectrometry (ICP-MS (NexION 300X; PerkinElmer)) analysis was performed before and after electrochemical sensing of $As^{3+}$. A Witec GmbH, Alpha-SNOM alpha300S confocal Raman instrument equipped with a 532 nm laser as the excitation source was used for Raman analysis. Measurements were carried out with a 20× objective (Plan-Apochromat, Zeiss), 600 grooves/mm grating, and at 1 s acquisition time. A laser power of ~10 mW was maintained on the sample during measurement. X-ray photoelectron spectroscopy (XPS) measurements were conducted using an Omicron Nanotechnology ESCA probe TPD spectrometer with polychromatic Al K$\alpha$ as the X-ray source ($h\nu$ = 1486.6 eV). $MnO_x$/ITO samples were mounted on a carbon tape, supported on the sample stub. A constant analyzer energy of 20 eV was used for the measurements. Binding energy was calibrated with respect to C 1s at 284.8 eV. All of the XPS spectra were deconvoluted using CasaXPS software.

## 3. RESULTS AND DISCUSSION

**3.1. Characterization by SEM and HRTEM.** Surface morphologies of the as-prepared $MnO_x$/ITO electrodes were analyzed using FESEM micrographs. Gold was sputtered on all electrodes prior to FESEM analyses. Difference in surface morphologies was observed in the electrodes prepared at three different CV potential windows. Also, there is a characteristic change in the morphologies at the nanoscale after using the electrode for $As^{3+}$ sensing (as seen in FESEM micrographs of Figure 1A,C).

Figure S2A,B in the Supporting Information (SI) shows the low- and high-magnification FESEM micrographs of as-prepared **M1** illustrating their surface morphology. Porous, globular structures (~800 nm to 1 $\mu$m diameter) with nanorod-like features diverging from the globular surface are observed on as-prepared electrode **M1**. This morphology is found to be similar to sea urchins. The entire electrode surface, including the surface of the spheres, is rough consisting of nanorods with uniform diameter and length. Song et al. have reported such sea urchin-shaped $MnO_2$ nanostructures prepared by the sodium dodecyl sulfate-assisted hydrothermal method.[35] Figure S2C,D shows FESEM micrographs of **M1** after $As^{3+}$ sensing. The nanorods, which were observed on the as-prepared electrode, were flattened after multiple stripping cycles of arsenic sensing.

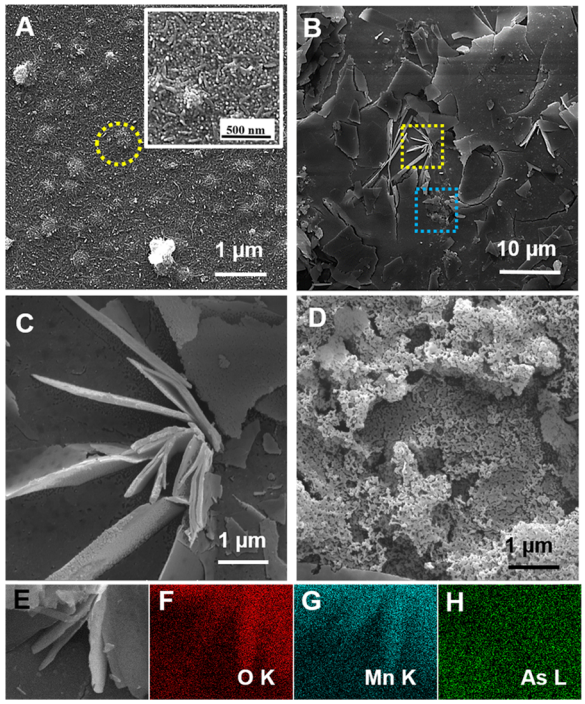


**Figure 1.** FESEM micrographs of (A) as-prepared **M3** and (B–D) after $As^{3+}$ sensing. The surface morphology before sensing (A) shows several globular structures (one such structure is marked by a yellow circle) embedded in a rough-surfaced mat of nanorods with the inset showing a high-magnification image. After $As^{3+}$ sensing, platelike structures (~5–10 $\mu$m diameter) as seen in (B) are observed all over the electrode surface. (C) and (D) are high-magnification micrographs. (C) Flower-shaped platelike structure (marked by the yellow square in (B)) and (D) porous surrounding morphology of the electrode (marked by blue square in (B)). (E) is the optical image, and (F)–(H) are the corresponding SEM–energy dispersive X-ray analysis maps for O, Mn, and As, respectively, after using **M3** for $As^{3+}$ sensing.

The **M2** appeared as flakes before sensing (Figure S3A,B), while after $As^{3+}$ sensing, dendritic structures (Figure S3C,D) were observed on the same electrode surface.

The FESEM micrograph of as-prepared electrode **M3** shows that the surface is covered with nanosized globular structures having a diameter of about 150–200 nm (Figure 1A). These are embedded in a hierarchical porous, spongy mat composed of an assembly of disordered nanorods. These $MnO_x$ nanorods can be seen clearly in the inset of Figure 1A, the diameter is approximately 20–40 nm, and the length of the nanorods is in the range of 150–200 nm. However, FESEM micrographs of the same electrode after $As^{3+}$ sensing show platelike structures shaped as flowers of ~5–10 $\mu$m diameter spread all over the electrode (Figure 1B). Figure 1C,D shows high-magnification micrographs showing one such structure and the porous nature of the electrode surface, respectively, obtained after $As^{3+}$ sensing. Figure 1E is the optical image, and Figure 1F–H shows the corresponding SEM–energy dispersive spectroscopy maps for O, Mn, and As elements after using electrode **M3** for $As^{3+}$ sensing. EDX analysis (shown in Figure S4) of the **M3** before and after $As^{3+}$ sensing shows the loss of manganese ions from the parent material, during stripping of $As^{3+}$.

Samples for HRTEM measurements were prepared by dispersing the electrodeposited $MnO_x$ layer from the electrode into ethanol by ultrasonication for 30 min. The dispersion was


DOI: 10.1021/acsami.9b06023
ACS Appl. Mater. Interfaces 2019, 11, 28154–28163

then spotted on a carbon-coated copper grid and dried under ambient conditions.

HRTEM analysis shows the polycrystalline nature of electrodeposited $MnO_x$. The morphology and lattice spacing of the electrode **M3** before and after $As^{3+}$ sensing are different, which is evident from the HRTEM micrographs shown in Figure 2. The HRTEM of as-prepared electrode (Figure 2A,B)

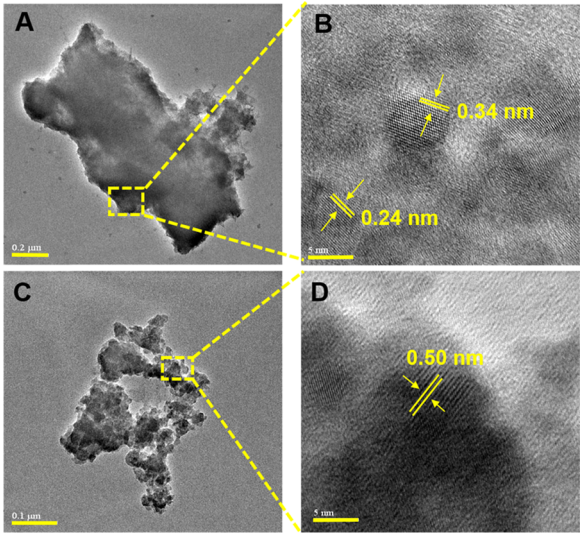


**Figure 2.** HRTEM micrographs of polycrystalline $MnO_x$ from **M3** (A, B) as-prepared electrode and (C, D) after $As^{3+}$ sensing. (A) and (C) are low-magnification images where (A) shows a large particle (~1.5 $\mu$m in length) and (C) shows a cluster of several nanosized particles of $MnO_x$. The high-magnification micrographs (B, D) show that the particles have definite lattice spacing before and after sensing. This signifies the phase transformation of as-prepared $MnO_x$ after $As^{3+}$ stripping. The scale bars are 0.2 $\mu$m, 5 nm, 0.1 $\mu$m, and 5 nm for (A), (B), (C), and (D), respectively.

shows that it is composed of larger particles with different lattice orientations. Moreover, there might be a possibility of nucleation of a mixed phase in the as-prepared samples. The lattice spacing of the sample after sensing (0.50 nm) changed drastically compared to that of the as-prepared sample (0.24 and 0.34 nm). This confirms the evolution of a new phase of the electrode material. The lattice spacing of the electrode after sensing corresponds to the $Mn_3O_4$ phase.[36] The lattice orientation and arrangement of $Mn_3O_4$ crystallites are almost unidirectional, which is observed in Figure 2D. The evolution of $Mn_3O_4$ after $As^{3+}$ sensing is presumably because of in situ growth of the material by successive deposition of $As^{3+}$ on $MnO/Mn_2O_3$ of the as-prepared electrode, followed by stripping of $As^{3+}$ from the electrode surface. During the deposition step of stripping voltammetry, there may be a formation of Mn−O−As complex due to weak interactions between Mn ions of the electrode and $As^{3+}$ ions from the electrolyte. Some of the Mn ions are released along with $As^{3+}$ during the anodic stripping step. In the subsequent stripping cycle, some Mn ions (present in the electrolyte due to the previous stripping cycle) may redeposit on the parent surface and, finally, get stripped out further with $As^{3+}$. It should be noted that the rates of desorption and deposition of Mn in the stripping cycles are different. This is confirmed by Mn and As ion analysis by ICP-MS. This successive desorption and deposition of Mn ions during LSSV cycles may be the cause for phase evolution of the parent material.

For the ICP-MS experiment, samples were collected from the electrolyte for ICP-MS analysis before performing LSSV ($As^{3+}$ sensing). The second-set samples for ICP-MS analysis were collected after the LSSV. This was repeated each time for different concentrations of $As^{3+}$ (1−100 ppb). The Mn ion release and As ion uptake by the electrode are indicated by the difference in concentrations of Mn and As ions before and after LSSV. We have analyzed the concentrations for three different **M3** electrodes. We observed that after each stripping step a minor change in the concentrations of manganese and arsenic ions is seen (Figure S5). The release of manganese ions from the electrode is more during the initial stripping cycles. The average concentration of manganese ions released into the electrolyte after each stripping cycle varies between 60 and 90 ppb. The uptake of arsenic by an electrode at each stripping cycle is less than ~2 ppb. This is not a significant change in concentration. However, this result proves that the electrode retains very less amount of arsenic after completion of a stripping voltammetric cycle. The arsenic deposited during the deposition step ($As^{3+}$ to $As^0$) is effectively getting stripped off during the anodic stripping step ($As^0$ to $As^{3+}$). Low arsenic retention by an electrode is beneficial for accurate results.

HRTEM micrographs of electrodes **M1** and **M2** (as-prepared and after $As^{3+}$ sensing) are given in Figures S6 and S7, respectively. Change in morphology and lattice spacing after $As^{3+}$ sensing was also observed in both these electrodes. HRTEM images of as-prepared **M1** and **M2** demonstrate nanorod-like structures with a lattice spacing of ~0.24 nm in Figures S6A,B and S7A,B. The morphology of electrode **M2** was changed to a crumpled paperlike structure after using it for sensing. The lattice spacings of **M1** (Figure S6C,D) and **M2** (Figure S7C,D) changed to ~0.24 and ~0.3 nm after sensing.

**3.2. X-ray Diffraction (XRD) Patterns, X-ray Photoelectron Spectroscopy (XPS), and Raman Spectral Analysis of Electrode M3.** The electrodeposited $MnO_x$ electrodes were air-dried and subsequently used directly for X-ray diffraction analysis. Figure 3A,B shows the XRD patterns obtained for **M3**. Crystallinity of the as-prepared $MnO_x$ sample was poor except that a diffraction peak of the electrodeposited material was observed at ~33.8° corresponding to either MnO, $Mn_2O_3$, or both (JCPDS file nos. 751090 and 894836 for MnO and $Mn_2O_3$, respectively). Manganese oxide-based compounds have $MnO_6$ octahedral units, which are connected by corner or edge sharing and form a structure with random intergrowth.[22,23] This is evident from the random lattice orientations in electron microscopy images (Figure 2B). There might also be a chance of coexistence of the mixed phase in the same sample, which has been discussed already in the HRTEM image analysis. The random arrangement of MnO/ $Mn_2O_3$ phase imparts different crystal orientations (Figure 2B) and demonstrate that they are not epitaxial in growth. The XRD patterns of the as-prepared $MnO/Mn_2O_3$ sample showed small diffraction peaks because of disorientation of the crystal planes, which can lead to diffused X-ray scattering. The sharp peaks, which are observed in Figure 3A, are mainly crystalline planes of the underlying ITO substrate (JCPDS file no: 71-2194) as shown in Figure S8A. However, the XRD features of the same electrode after $As^{3+}$ stripping (Figure 3B) differ distinctly from those of the as-prepared samples. There is an evolution of a new phase after $As^{3+}$ stripping, which is confirmed by the sharp diffraction peaks ($2\theta$ ~ 16, 32.3, and 49°) in the XRD pattern shown in Figure 3B. The peaks correspond to $Mn_3O_4$ (JCPDS file 894837). The


DOI: 10.1021/acsami.9b06023
ACS Appl. Mater. Interfaces 2019, 11, 28154−28163

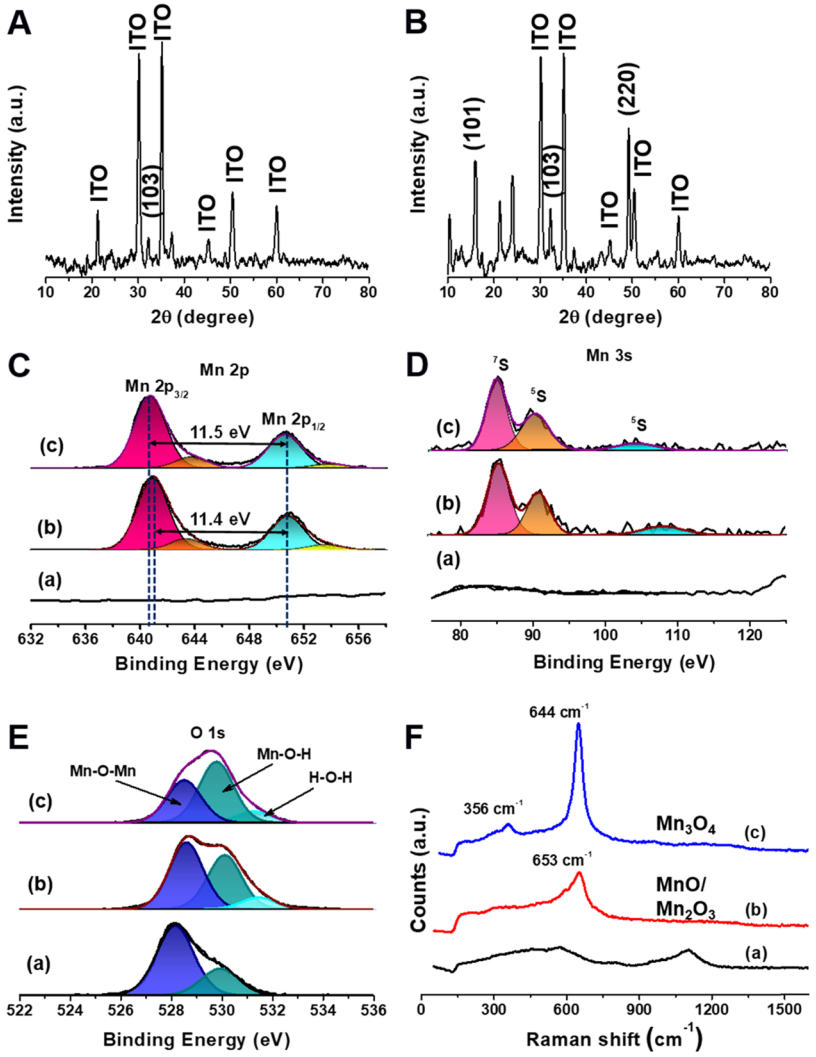


**Figure 3.** Characterization of electrode **M3**: (A) and (B) are XRD patterns of **M3**. The (*hkl*) planes are indicated. Planes for the as-prepared electrode correspond to the (A) MnO or $Mn_2O_3$ phase and (B) $Mn_3O_4$ after $As^{3+}$ sensing. The unassigned peaks correspond to the XRD pattern of the ITO glass substrate, which are mentioned in Figure S8A. The data were recorded using a Cu K$\alpha$ source. (C), (D), and (E) are XPS data of the Mn 2p, Mn 3s, and O 1s regions, respectively. (F) Raman spectra of electrode **M3**. (a), (b), and (c) in (C)−(F) correspond to bare ITO, as-prepared $MnO_x$ electrodes (before sensing), and $MnO_x$ electrodes after sensing, respectively.

evolution into $Mn_3O_4$ is governed by the successive electrochemical adsorption and desorption of $As^{3+}$ during deposition and stripping events of the LSSV cycle, respectively. During the deposition step of $As^{3+}$ on manganese oxide, there may be a formation of Mn−O−As species on the electrode surface because of the scavenging effect of $MnO_x$ toward $As^{3+}$. Subsequently, during the $As^{3+}$ stripping step, the release of manganese ions with $As^{3+}$ (dissolution−reprecipitation of manganese) may change the oxidation states or phase of parent $MnO/Mn_2O_3$. Initial degradation of the manganese oxide surface during stripping voltammetry leads to the formation of a new microstructure along with the phase evolution to $Mn_3O_4$. To verify the conjecture whether $As^{3+}$ has a role in the evolution of the new material or not, we have performed a control experiment. For that, LSSV was performed on **M3** in two different electrolytes: distilled water and PBS. This was followed by washing the electrode with distilled water (without $As^{3+}$) and, subsequently, XRD data were taken (Figure S8B). No additional XRD peak was observed after performing LSSV in the absence of $As^{3+}$ in both distilled water and PBS.

To get more insight into the oxidation states of Mn, we have performed XPS of the as-prepared electrodeposited electrodes. XPS data of the Mn 2p, O 1s, As 3d, and Mn 3s regions were measured before and after As sensing to understand the effect of LSSV on the oxidation state of electrodeposited $MnO_x$. The Mn 2p spectra (Figure 3C) of both, before and after sensing, $MnO_x$ electrodes exhibit a spin−orbit doublet composed of Mn $2p_{3/2}$ and Mn $2p_{1/2}$ peaks. A slight change in the $\Delta J$ values of 11.4 and 11.5 eV was observed for electrodes before and after sensing, respectively. Both Mn $2p_{3/2}$ and Mn $2p_{1/2}$ peaks were deconvoluted for both the samples. The Mn $2p_{3/2}$ peak of the as-prepared $MnO_x$ electrode is observed at 640.4 eV, which is the main characteristic peak of $Mn^{3+}$.[37] The Mn $2p_{3/2}$ peak of the same electrode after electrochemical sensing exhibited a small shift in binding energy (640 eV). Mn 3s spectra (Figure 3D) of the electrode before and after sensing were also analyzed to get more information about the oxidation states of Mn. The splitting of Mn 3s spectra arises from exchange interaction between the unpaired electrons in the 3s orbital and the 3d valence band electrons.[38] Splitting energy of the Mn 3s spectrum (5.4 eV between $^7S$ and $^5S$ states) affirms the


DOI: 10.1021/acsami.9b06023
ACS Appl. Mater. Interfaces 2019, 11, 28154−28163

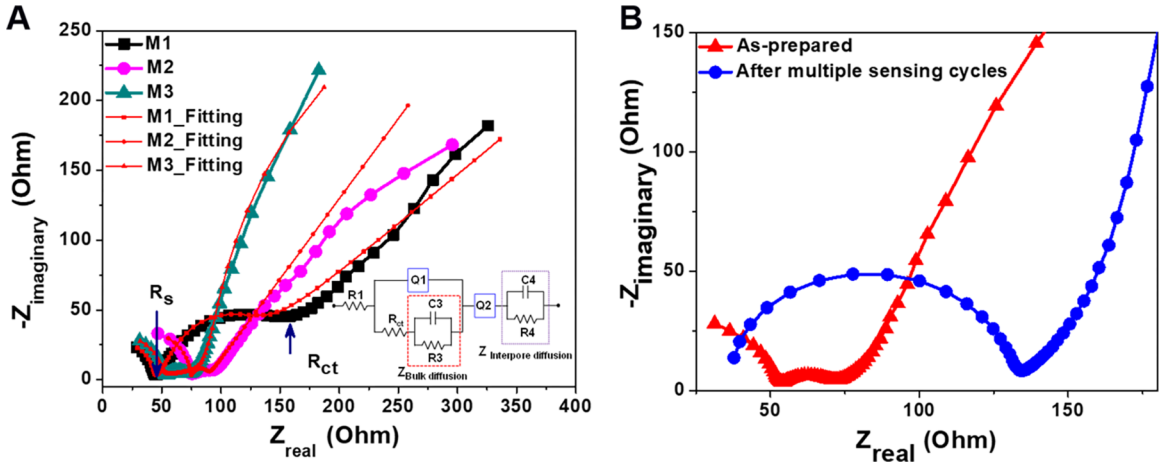


**Figure 4.** (A) Nyquist plots of electrochemical impedance spectra for $MnO_x$/ITO electrodes (**M1**, **M2**, and **M3**) in PBS. Each Nyquist plot can be fitted with the same electronic circuit shown in the inset. The value of each component is different for each electrode and is shown in Table S1. The electronic components have their individual significance in the electrochemical process. (B) A comparative study of the Nyquist plot for as-prepared **M3** and the same electrode after multiple stripping cycles for arsenic sensing.

$Mn^{3+}$ oxidation state of the electrode before electrochemical sensing.[19,39] The splitting energy of 5.5 eV of the same electrode after electrochemical sensing corresponds to the $Mn_3O_4$ phase, which is consistent with previous reports.[38,39]

The O 1s spectra (Figure 3E) of the electrode, before and after sensing, showed a broad peak, which was deconvoluted into three peaks. The peak at 528 eV belongs to the Mn−O−Mn binding energy, the peak at 530 eV corresponds to hydroxyl groups attached to manganese (Mn−OH), and the 531 eV peak belongs to water or hydroxyl groups, which were physically adsorbed on the surface of the electrode. After sensing, there is a significant rise in the 530 eV peak compared to the 528 eV peak; this attributes to hydration of surface Mn−O−Mn groups. No peak was observed in the As 3d region of 44−46 eV (As(III)/As(V)) before and after sensing (Figure S9). Thus, there is no considerable amount of arsenic binding to the surface after multiple stripping cycles of As sensing.

To get more profound insights into the phase evolution of the initially deposited material, we have performed Raman spectroscopy measurements on electrode **M3**, before and after $As^{3+}$ sensing along with a bare ITO substrate as a control. The spectra are shown in Figure 3F. Raman spectrum of the as-prepared sample (spectrum b) shows the main characteristic peak at 653 $cm^{-1}$, which corresponds to the symmetric stretching of the Mn−O−Mn bond of $MnO_6$ octahedron of $MnO/Mn_2O_3$. This is in good agreement with the previous reports.[40] However, after electrochemical arsenic sensing, the same sample exhibits a relatively higher-intensity Raman peak at 646 $cm^{-1}$ with a blue shift of the vibrational frequency of the symmetric stretching mode of $MnO_6$ octahedron. Distortion of the $MnO_6$ octahedron resulting from the formation of Mn−O−As species during deposition of $As^{3+}$ in LSSV cycles leads to a blue shift. Furthermore, the release of manganese along with $As^{3+}$ into the electrolyte leads to the appearance of a lower-frequency peak at 357 $cm^{-1}$ due to the deformation mode of the Mn−O chain in the $MnO_6$ octahedron. This results suggests the evolution of the material with a new oxidation state corresponding to $Mn_3O_4$. The release of manganese ions along with $As^{3+}$ during multiple stripping cycles is supported by SEM−EDX elemental analysis (Figure S4) and ICP-MS analysis (Figure S5) of the **M3** before and after $As^{3+}$ stripping.

**3.3. Electrochemical Impedance Spectroscopy Studies on $MnO_x$ Electrodes.** Electrochemical properties including interfacial charge transport characteristics at the electrode−electrolyte interface largely depend upon the phase and electronic conductivity of the electrode material, while bulk diffusion and interpore diffusion are influenced by the hierarchical surface morphology of each $MnO_x$/ITO electrode. The electrochemical properties at the electrode surface can be viewed as a nonlinear phenomenon, and each phenomenon can be estimated in terms of electronic components (resistor, capacitor, and constant phase element) of a nonlinear electronic circuit. Thus, an impedance spectrum simulated from an alternating current (AC) perturbation applied to a nonlinear electronic circuit can be fitted with the experimental impedance spectrum obtained from EIS measurements of an individual electrode. Electronic properties of as-prepared $MnO_x$/ITO electrodes electrodeposited at different potential windows and their influence on the electrochemical properties were analyzed by EIS. An AC signal of 10 mV was applied to the $MnO_x$/ITO electrode with respect to the reference electrode, and subsequently, the current was measured between working and counter electrodes. EIS was carried out in PBS electrolyte, and impedance was recorded at each frequency of the AC signal, which was varied from 200 kHz to 100 mHz at 6 dB per decade.

In the complex impedance (Nyquist) plot shown in Figure 4A, the semicircle describes the interfacial electron transport property of the $MnO_x$/ITO electrode, while the straight line after the semicircle is known as Warburg impedance. This corresponds to the diffusion of bulk ions to the electrode−electrolyte interface. Each semicircle of the electrode consists of two intercepts; the first intercept is related to the equivalent series resistance ($R_S$) between $MnO_x$ and current collector (here ITO), while the second intercept is associated with the charge transfer resistance ($R_{ct}$) from the electrolyte to the $MnO_x$ electrode through the Faradaic redox reaction. The $R_S$ and $R_{ct}$ for electrode **M1** are indicated in Figure 4A. Summary of these two resistances of all of the samples and EIS spectra recorded for the bare ITO glass substrate are presented in Table 1 and Figure S10, respectively. The inset in Figure 4A is the corresponding electronic circuit for the Nyquist plot. Parallel combinations of both C3−R3 and C4−R4 are


DOI: 10.1021/acsami.9b06023
ACS Appl. Mater. Interfaces 2019, 11, 28154−28163

**Table 1. Summary of Equivalent Series Resistance ($R_S$) and Charge Transfer Resistance ($R_{ct}$) of Different $MnO_x$/ITO Electrodes Obtained from EIS Measurements**

| electrodeposition voltage window | equivalent series resistance ($R_S$) ($MnO_x$ to ITO) (Ω) | charge transfer resistance ($R_{ct}$) (electrolyte to $MnO_x$) (Ω) |
|---|---|---|
| **M1** (0.8−1.3 V) | 44 | 115 |
| **M2** (−0.2−0.9 V) | 74 | 23 |
| **M3** (−1−1.3 V) | 53 | 23 |

impedances that are related to diffusion of ions from the bulk electrolyte into the hierarchical rough surface of the as-prepared electrode. Q1 and Q2 are called constant phase elements, which are associated with the double-layer capacitance formed in the inter-/intraparticle rough surface of the electrode. The values of these components for electrodes **M1**, **M2**, and **M3** are given in Table S1. From the Nyquist plot (Figure 4A) and Table S1, we observe that both bulk diffusion and interpore diffusion on the surface of **M1**, **M2**, and **M3** are almost similar. Therefore, the differences in the surface morphologies of electrodes do not affect the ion diffusion toward the electrode surface. However, a significant change in $R_{ct}$ (~23 Ω) is observed at the electrode−electrolyte interface of **M3** compared to **M1** and **M2**. Electrode **M1** exhibited the highest $R_{ct}$ among all three electrodes and has poor response to arsenic sensing although it showed lowest $R_S$. Thus, redox reactions occur faster on the **M3** electrode surface during stripping voltammetry (Figure 5B). On the other hand, electrode **M2** showed almost the same $R_{ct}$ as compared to electrode **M3**, but its high $R_S$ hinders the arsenic sensing response for higher arsenic concentrations. However, the $R_S$ of **M2** is highest compared to the other electrodes. Here, we would like to mention that $R_S$ is the combination of both solution (or electrolyte) resistance and material's internal resistance. Since we have used the same electrolyte (PBS) during EIS measurements, any change in $R_S$ is because of the change in electronic conductivity of the electrode material. For electrochemical sensor applications, the electrode must have low series and charge transfer resistances. Since electrode **M3** has lower internal resistance and it promotes better charge transfer compared to the other electrodes, this electrode is the best choice for sensing applications. The interfacial charge transfer property is a crucial factor for an electrochemical sensor as it directly influences the arsenite sensing response by the electrodes. Electrode **M3** is a better choice in terms of this property too.

EIS of **M3** before and after $As^{3+}$ sensing was also studied, and the corresponding results are shown in Figure 4B. After multiple stripping cycles for $As^{3+}$ sensing, the internal resistance of **M3** is lowered; however, there was an increase in the interfacial charge transfer resistance at the electrode−electrolyte interface. The decrease in the internal resistance of electrode may be attributed to the phase evolution of the crystalline $Mn_3O_4$ phase with unidirectional lattice orientation (Figure 2D) after $As^{3+}$ sensing. Since manganese is released into the electrolyte with $As^{3+}$ stripping, the effective electrochemical surface area of **M3** is reduced, and as a result, an increase in charge transfer resistance is observed.

### 3.4. Electrochemical Analysis for Arsenite ($As^{3+}$) Sensing Using Optimized Electrode M3 and Determi-

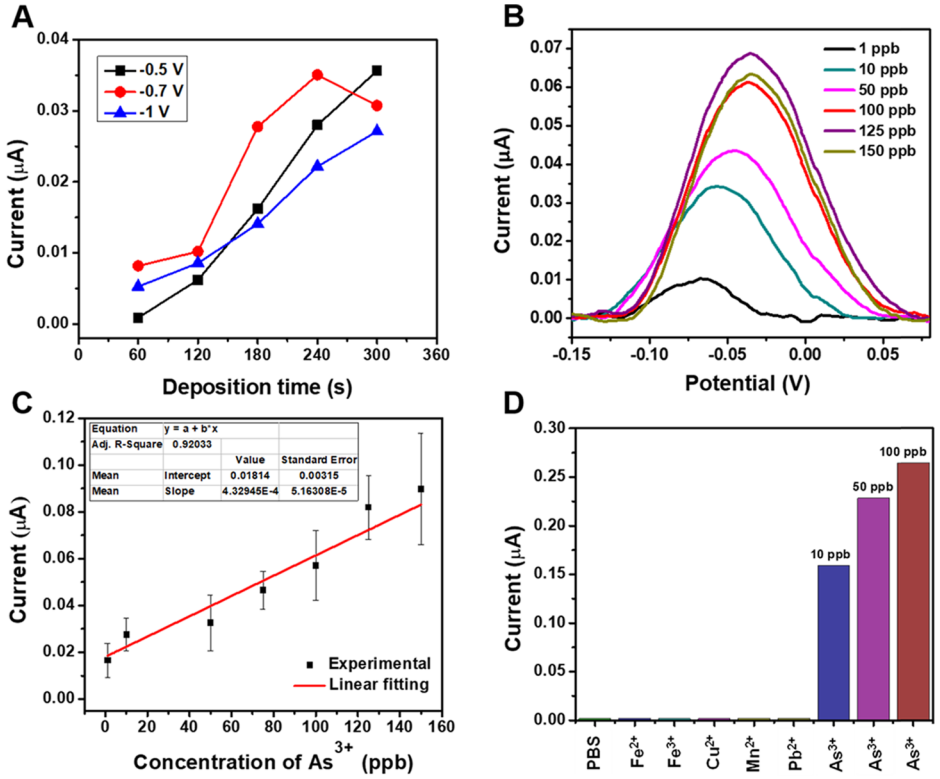


**Figure 5.** Electrochemical arsenite sensing by **M3** in PBS: (A) optimization of deposition potential and time for $As^{3+}$ sensing. (B) LSSV response for various concentrations (1−150 ppb) of $As^{3+}$. (C) Linearity analysis of chronoamperometric current for different concentrations of $As^{3+}$. Error bars represent interelectrode variability. (D) Interfering ions study with different metal ions (100 ppb $Fe^{2+}$, $Fe^{3+}$, $Cu^{2+}$, $Mn^{2+}$, and $Pb^{2+}$ added sequentially) and the response of arsenic in the presence of all of the metal ions using **M3**.



DOI: 10.1021/acsami.9b06023
ACS Appl. Mater. Interfaces 2019, 11, 28154−28163

**nation of Limit of Detection (LOD) through Linear Response to $As^{3+}$ by the Electrode.** To obtain the best performance for detection of trace amount of $As^{3+}$ in water with our $MnO_x$/ITO electrode, crucial experimental parameters like deposition potential (DP) and deposition time (DT) were optimized. PBS was used as the electrolyte during all of the LSSV measurements. For optimization, we varied DT from 60 to 300 s at a constant DP and concentration of arsenic. Subsequently, the stripping current peak was monitored. This was repeated for three DPs of −0.5, −0.7, and −1 V at 10 ppb $As^{3+}$. Figure 5A shows the peak current as a function of DT. It is observed that the stripping current at each DT is higher for −0.7 V compared to other DPs and that it reaches a maximum at 240 s. Thus, the parameters of −0.7 V and 180 s were selected as DP and DT, respectively, for stripping voltammetry. For arsenite sensing, the stripping current was recorded at these optimized parameters during the anodic potential sweep with different concentrations of $As^{3+}$. Arsenite concentration as low as 1 ppb was experimentally detected by LSSV using electrodes prepared at all of the three voltage windows of deposition (**M1**, **M2**, and **M3**). However, the current intensity of the $As^{3+}$ peak is different for each of the three electrodes. The electrode **M3** exhibited the best $As^{3+}$ sensing behavior with linear concentration-dependent response over the concentration range of 1−150 ppb. Figure 5B illustrates the LSSV signal of electrode **M3** for various concentrations of $As^{3+}$ in PBS. However, Figure S11A,B show the LSSV signal for $As^{3+}$ by electrodes **M1** and **M2**, respectively.

The electrochemical analysis revealed that the electrode **M3** has a higher electrochemical activity toward $As^{3+}$. The limit of detection (LOD) obtained experimentally using our $MnO_x$ electrode was 1 ppb. Researchers have reported theoretical LODs of 0.825 ppb using $CoO_x$ on a glassy carbon electrode in PBS of pH 7,[41] 0.1 ppb using a rGO/$MnO_2$ nanohybrid on glassy carbon electrodes in acetate buffer of pH 5,[13] etc. However, one interesting aspect of our experiment is that we have carried out electrochemical analysis through LSSV at slightly basic pH (∼7.4), which leads to the practical viability in field water analysis. Furthermore, arsenic dissolution in a basic pH electrolyte does not generate toxic arsine gas, which is produced when arsenic is dissolved in an acidic medium.

The saturation concentration of $As^{3+}$ is different for the three different electrodes (**M1**, **M2**, and **M3**). As shown in Figure 5B, the response of **M3** was saturated at ∼125−150 ppb, while **M1** (Figure S10A) and **M2** (Figure S10B) were saturated at ∼100−110 and ∼60−70 ppb $As^{3+}$, respectively. The linear response of **M3** is shown in Figure 5C. The data is recorded with three different **M3** electrodes. Error bars represent interelectrode variability. The stripping current varied linearly with the concentration of $As^{3+}$ over the range of 1−150 ppb. The eventual decrease in sensitivity observed after multiple stripping cycles may be explained by the change in electronic properties (wherein the active material converts into $Mn_3O_4$ from as-prepared $MnO/Mn_2O_3$) as reported in EIS studies. The current response is fitted with the linear regression equation of $y = 0.0004x + 0.018$ (where $y$ is the sensor response current and $x$ is the $As^{3+}$ concentration), and the regression correlation coefficient was 0.92. The theoretical LOD was 0.012 ppb, and the calculation is given in formulas 1 and 2 of SI.

The electrodes **M1**, **M2**, and **M3** showed different sensing behaviors for various $As^{3+}$ concentrations (data for **M1** and **M2** are shown in Figure S11A,B, respectively). Different sensing results by the three electrodes are influenced by their individual material properties such as morphology, phase, and interfacial charge transfer.

A control experiment was performed to check the impact of the optimized parameters on the electrochemical performance of the bare ITO electrode. For this, cyclic voltammetry was performed on the bare ITO electrode using a redox molecule before and after performing stripping voltammetry (at optimized parameters in PBS). CV measurements confirmed that there is no significant change in redox peaks even after application of −0.7 V for 180 s for ten LSSV cycles. These experimental results support the electrochemical stability of ITO and absence of electrochemical hindrance at the electrode−electrolyte interface. The corresponding cyclic voltammogram is given in Figure S12.

Interference study with different metal ions (shown in Figure 5D) using electrode **M3** was performed in PBS. The concentration of all of the metal ions ($Fe^{2+}$, $Fe^{3+}$, $Cu^{2+}$, $Mn^{2+}$, and $Pb^{2+}$) was maintained at 100 ppb during the study. Later, three arsenic concentrations (10, 50, and 100 ppb) were analyzed in the presence of these metals. The metal ions were added sequentially, as represented in Figure 5D. Stripping voltammetry was performed for all metal ions keeping the deposition potential constant at −0.7 V, and stripping of the ions was performed within the fixed potential window (−0.40−0.20 V). The peak potential and current were monitored for each ion. Electrode **M3** was inert toward both $Fe^{2+}$ and $Fe^{3+}$ ions, and an absence of peak current was seen. A peak current was registered with $Cu^{2+}$, $Mn^{2+}$, and $Pb^{2+}$ at the oxidation potential value of −0.17 V for $Cu^{2+}$ and $Mn^{2+}$ and −0.18 V for $Pb^{2+}$. Moreover, the current intensity of the $Mn^{2+}$ peak was higher as compared to that of $Cu^{2+}$ at the same potential. There is no interference of metal ions at the oxidation potential of $As^{3+}$ and hence electrode **M3** is highly selective for $As^{3+}$ detection. Enhancement of the oxidation current of $As^{3+}$ was observed with a sequential increase of $As^{3+}$ concentration in the presence of all metal ions.

The probable mechanism for phase evaluation of the active material during sensing may be explained by the following chemical reactions.

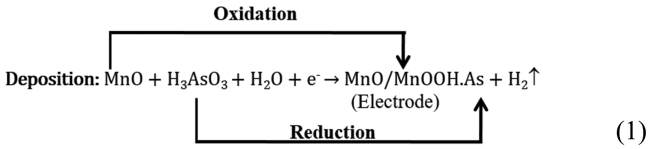


(1)

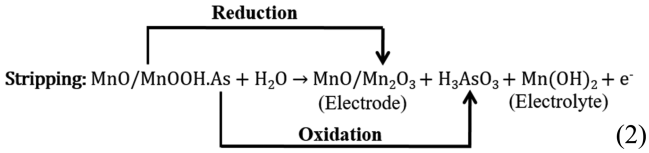


(2)

Phase evolution:

$$MnO/Mn_2O_3 + Mn(OH)_2 + e^- \rightarrow \underset{\text{(electrode)}}{Mn_3O_4} + H_2\uparrow \quad (3)$$

Electrochemical sensing of arsenic by the as-prepared electrode and subsequent phase evolution of the parent material after sensing involve various reaction steps. In the deposition step of LSSV (eq 1), electrodeposited $MnO_x$ gets oxidized ($Mn^{2+}$ to $Mn^{3+}$) and $As^{3+}$ from the electrolyte is reduced to $As^0$ on the electrode. The Mn−O−As complex thus formed may exist as


DOI: 10.1021/acsami.9b06023
ACS Appl. Mater. Interfaces 2019, 11, 28154−28163

MnOOH·As species on the parent $MnO_x$ electrode. During the subsequent stripping step, $As^0$ is stripped out from the electrode in an oxidized form ($As^{3+}$) into the electrolyte. Concomitantly, some manganese ions are also released into the electrolyte (as proved from ICP-MS data, Figure S5B) in the form of $Mn(OH)_2$ along with $As^{3+}$. This leads to the evolution of a new phase ($Mn_2O_3$) on the parent $MnO_x$ material. The phase evolution occurs gradually over successive LSSV cycles. Some of the manganese ions in the electrolyte ($Mn(OH)_2$) get redeposited on the electrode surface during subsequent LSSV cycles, eventually leading to the formation of $Mn_3O_4$. This is supported by both XPS and Raman spectroscopy.

## 4. CONCLUSIONS

This study established a simple, fast, efficient, and non-enzymatic electrochemical technique for $As^{3+}$ detection. The cyclic-voltammetry-based electrodeposition method is demonstrated for $MnO_x$/ITO electrode preparation and its application in the detection of trace amount of arsenite (~1 ppb) in an aqueous electrolyte via linear sweep stripping voltammetry. Detailed characterization of $MnO_x$ samples before and after LSSV confirmed the evolution of a new phase along with the appearance of new morphology of the active material. In situ growth of the new phase on the electrode was observed during stripping voltammetry. The experimental limit of detection (LOD) of 1 ppb obtained by the $MnO_x$/ITO electrode is well below the guideline value for As(III) in drinking water (10 ppb) as specified by the World Health Organization (WHO). The advantages of this electrode are its suitability for $As^{3+}$ sensing with significant sensitivity, selectivity, low LOD, reproducibility, and importantly low cost. Moreover, the electrode is capable of interference-free $As^{3+}$ detection in alkaline medium.

## ■ ASSOCIATED CONTENT

### Supporting Information

The Supporting Information is available free of charge on the ACS Publications website at DOI: 10.1021/acsami.9b06023.

Values of each component of the electronic circuit used to fit Nyquist plots of EIS for **M1**, **M2**, and **M3** electrodes; Pourbaix diagram (Eh−pH) of various forms of manganese oxide and hydroxide; characterization of electrodes **M1** and **M2** including FESEM, EDX, TEM, and XRD; ICP-MS data for change in As and Mn ion concentrations in the electrolyte for **M3**; Nyquist plot of bare ITO; response of $As^{3+}$ using electrodes **M1** and **M2**; CV of bare ITO at optimized parameters; and calculation of LOD (PDF)

## ■ AUTHOR INFORMATION


### Corresponding Authors

*E-mail: tijuthomas@iitm.ac.in (T.T.).
*E-mail: pradeep@iitm.ac.in (T.P.).

### ORCID

Sourav Kanti Jana: 0000-0001-5772-7022
Pillalamarri Srikrishnarka: 0000-0001-5187-6879
Thalappil Pradeep: 0000-0003-3174-534X


### Author Contributions

§T.G. and S.K.J. contributed equally.

### Notes

The authors declare no competing financial interest.

## ■ ACKNOWLEDGMENTS

The authors thank the Department of Science and Technology, Government of India, for supporting our research program. T.G., S.K.J., P.S., S.M., T.A., and C.S. thank IIT Madras for their fellowships. J.S.M. thanks the CSIR for research fellowship. The authors thank the Centre for Nano and Soft Matter Sciences (CeNS) for their FESEM facility.

## ■ REFERENCES


(1) Ravenscroft, P. *Predicting the Global Extent of Arsenic Pollution of Groundwater and Its Potential Impact on Human Health*; UNICEF: New York, 2007.
(2) Gómez-Ariza, J. L.; Sánchez-Rodas, D.; Giráldez, I.; Morales, E. A Comparison between ICP-MS and AFS Detection for Arsenic Speciation in Environmental Samples. *Talanta* **2000**, *51*, 257−268.
(3) WHO. *Guidelines for Drinking-Water Quality*; WHO, 2011; pp 315−318.
(4) USEPA. *Technical Factsheet: Final Rule for Arsenic in Drinking Water*; USEPA, 2001; pp 1−6.
(5) International Agency for Research on Cancer (IARC). Arsenic and Arsenic Compounds Monograph. *IARC Monogr. Eval. Carcinog. Risks Hum.* **2012**, *100C*, 41−93.
(6) Bibi, S.; Kamran, M. A.; Sultana, J.; Farooqi, A. Occurrence and Methods to Remove Arsenic and Fluoride Contamination in Water. *Environ. Chem. Lett.* **2017**, *15*, 125−149.
(7) Masscheleyn, P. H.; Delaune, R. D.; Patrick, W. H. Effect of Redox Potential and PH on Arsenic Speciation and Solubility in a Contaminated Soil. *Environ. Sci. Technol.* **1991**, *25*, 1414−1419.
(8) Fish, R. H.; Brinckman, F. E.; Jewett, K. L. Fingerprinting Inorganic Arsenic and Organoarsenic Compounds in in Situ Oil Shale Retort and Process Waters Using a Liquid Chromatograph Coupled with an Atomic Absorption Spectrometer as a Detector. *Environ. Sci. Technol.* **1982**, *16*, 174−179.
(9) Luong, J. H. T.; Majid, E.; Male, K. B. Analytical Tools for Monitoring Arsenic in the Environment. *Open Anal. Chem. J.* **2007**, *1*, 7−14.
(10) Male, K. B.; Hrapovic, S.; Santini, J. M.; Luong, J. H. T. Biosensor for Arsenite Using Arsenite Oxidase and Multiwalled Carbon Nanotube Modified Electrodes. *Anal. Chem.* **2007**, *79*, 7831−7837.
(11) Fuku, X.; Iftikar, F.; Hess, E.; Iwuoha, E.; Baker, P. Cytochrome c Biosensor for Determination of Trace Levels of Cyanide and Arsenic Compounds. *Anal. Chim. Acta* **2012**, *730*, 49−59.
(12) Merulla, D.; Buffi, N.; Beggah, S.; Truffer, F.; Geiser, M.; Renaud, P.; Van der Meer, J. R. Bioreporters and Biosensors for Arsenic Detection. Biotechnological Solutions for a World-Wide Pollution Problem. *Curr. Opin. Biotechnol.* **2013**, *24*, 534−541.
(13) Devi, P.; Bansod, B.; Kaur, M.; Bagchi, S.; Nayak, M. K. Co-Electrodeposited RGO/MnO2 Nanohybrid for Arsenite Detection in Water by Stripping Voltammetry. *Sens. Actuators B Chem* **2016**, *237*, 652−659.
(14) Jiang, T. J.; Guo, Z.; Liu, J. H.; Huang, X. J. Gold Electrode Modified with Ultrathin SnO2 Nanosheets with High Reactive Exposed Surface for Electrochemical Sensing of As(III). *Electrochim. Acta* **2016**, *191*, 142−148.
(15) Yang, M.; Chen, X.; Jiang, T. J.; Guo, Z.; Liu, J. H.; Huang, X. J. Electrochemical Detection of Trace Arsenic(III) by Nanocomposite of Nanorod-Like α-MnO2 Decorated with ~5 Nm Au Nanoparticles: Considering the Change of Arsenic Speciation. *Anal. Chem.* **2016**, *88*, 9720−9728.
(16) Ivandini, T. A.; Sato, R.; Makide, Y.; Fujishima, A.; Einaga, Y. Electrochemical Detection of Arsenic(III) Using Iridium-Implanted Boron-Doped Diamond Electrodes. *Anal. Chem.* **2006**, *78*, 6291−6298.
(17) March, G.; Nguyen, T. D.; Piro, B. Modified Electrodes Used for Electrochemical Detection of Metal Ions in Environmental Analysis. *Biosensors* **2015**, *5*, 241−275.

(18) Bhanjana, G.; Dilbaghi, N.; Chaudhary, S.; Kim, K. H.; Kumar, S. Robust and Direct Electrochemical Sensing of Arsenic Using Zirconia Nanocubes. *Analyst* **2016**, *141*, 4211−4218.
(19) Saha, B.; Jana, S. K.; Majumder, S.; Satpati, B.; Banerjee, S. Selective Growth of Co-Electrodeposited Mn2O3-Au Spherical Composite Network Towards Enhanced Non-Enzymatic Hydrogen Peroxide Sensing. *Electrochim. Acta* **2015**, *174*, 853−863.
(20) Panagiotopoulos, A.; Gkouma, A.; Vassi, A.; Johnson, C. J.; Cass, A. E. G.; Topoglidis, E. Hemin Modified SnO2 Films on ITO-PET with Enhanced Activity for Electrochemical Sensing. *Electroanalysis* **2018**, *30*, 1956−1964.
(21) Xiao, L.; Wildgoose, G. G.; Compton, R. G. Sensitive Electrochemical Detection of Arsenic (III) Using Gold Nanoparticle Modified Carbon Nanotubes via Anodic Stripping Voltammetry. *Anal. Chim. Acta* **2008**, *620*, 44−49.
(22) Aghazadeh, M.; Maragheh, M. G.; Ganjali, M. R.; Norouzi, P.; Faridbod, F. Electrochemical Preparation of MnO2 Nanobelts through Pulse Base-Electrogeneration and Evaluation of Their Electrochemical Performance. *Appl. Surf. Sci.* **2016**, *364*, 141−147.
(23) Zhang, K.; Han, X.; Hu, Z.; Zhang, X.; Tao, Z.; Chen, J. Nanostructured Mn-Based Oxides for Electrochemical Energy Storage and Conversion. *Chem. Soc. Rev.* **2015**, *44*, 699−728.
(24) Schacht, L.; Ginder-Vogel, M. Arsenite Depletion by Manganese Oxides: A Case Study on the Limitations of Observed First Order Rate Constants. *Soil Syst.* **2018**, *2*, 39.
(25) Zhang, G. S.; Qu, J. H.; Liu, H. J.; Liu, R. P.; Li, G. T. Removal Mechanism of As(III) by a Novel Fe-Mn Binary Oxide Adsorbent: Oxidation and Sorption. *Environ. Sci. Technol.* **2007**, *41*, 4613−4619.
(26) Maliyekkal, S. M.; Philip, L.; Pradeep, T. As(III) Removal from Drinking Water Using Manganese Oxide-Coated-Alumina: Performance Evaluation and Mechanistic Details of Surface Binding. *Chem. Eng. J.* **2009**, *153*, 101−107.
(27) Dalvi, A. A.; Ajith, N.; Swain, K. K.; Verma, R. Sorption of Arsenic on Manganese Dioxide Synthesized by Solid State Reaction. *J. Environ. Sci. Health, Part A: Toxic/Hazard. Subst. Environ. Eng.* **2015**, *50*, 866−873.
(28) McKenzie, R. M. The Synthesis of Birnessite, Cryptomelane, and Some Other Oxides and Hydroxides of Manganese. *Mineral. Mag.* **1971**, *38*, 493−502.
(29) Zhou, S.; Han, X.; Fan, H.; Liu, Y. Electrochemical Sensing toward Trace As(III) Based on Mesoporous MnFe2O4/Au Hybrid Nanospheres Modified Glass Carbon Electrode. *Sensors* **2016**, *16*, No. 935.
(30) Wu, S.; Zhao, Q.; Zhou, L.; Zhang, Z. Stripping Analysis of Trace Arsenic Based on the MnOx/ AuNPs Composite Film Modified Electrode in Alkaline Media. *Electroanalysis* **2014**, *26*, 1840−1849.
(31) Bu, L.; Gu, T.; Ma, Y.; Chen, C.; Tan, Y.; Xie, Q.; Yao, S. Enhanced Cathodic Preconcentration of As(0) at Au and Pt Electrodes for Anodic Stripping Voltammetry Analysis of As(III) and As(V). *J. Phys. Chem. C* **2015**, *119*, 11400−11409.
(32) Salimi, A.; Hyde, M. E.; Banks, C. E.; Compton, R. G. Boron Doped Diamond Electrode Modified with Iridium Oxide for Amperometic Detection of Ultra Trace Amounts of Arsenic(III). *Analyst* **2004**, *129*, 9−14.
(33) Granqvist, C. G.; Hultåker, A. Transparent and Conducting ITO Films: New Developments and Applications. *Thin Solid Films* **2002**, *411*, 1−5.
(34) Freitas, R. M.; Perilli, T. A. G.; Ladeira, A. C. Q. Oxidative Precipitation of Manganese from Acid Mine Drainage by Potassium Permanganate. *J. Chem.* **2013**, *2013*, 1−8.
(35) Song, X. C.; Zhao, Y.; Zheng, Y. F. Synthesis of MnO2 Nanostructures with Sea Urchin Shapes by a Sodium Dodecyl Sulfate-Assisted Hydrothermal Process. *Cryst. Growth Des.* **2007**, *7*, 159−162.
(36) Song, R.; Feng, S.; Wang, H.; Hou, C. Effect of Organic Solvents on Particle Size of Mn3O4 Nanoparticles Synthesized by a Solvothermal Method. *J. Solid State Chem.* **2013**, *202*, 57−60.
(37) Kar, P.; Sardar, S.; Ghosh, S.; Parida, M. R.; Liu, B.; Mohammed, O. F.; Lemmens, P.; Pal, S. K. Nano Surface Engineering of Mn2O3 for Potential Light-Harvesting Application. *J. Mater. Chem. C* **2015**, *3*, 8200−8211.
(38) Lee, J. W.; Hall, A. S.; Kim, J. D.; Mallouk, T. E. A Facile and Template-Free Hydrothermal Synthesis of Mn3O4 Nanorods on Graphene Sheets for Supercapacitor Electrodes with Long Cycle Stability. *Chem. Mater.* **2012**, *24*, 1158−1164.
(39) Wu, T. H.; Hesp, D.; Dhanak, V.; Collins, C.; Braga, F.; Hardwick, L. J.; Hu, C. C. Charge Storage Mechanism of Activated Manganese Oxide Composites for Pseudocapacitors. *J. Mater. Chem. A* **2015**, *3*, 12786−12795.
(40) Julien, C. M.; Massot, M.; Poinsignon, C. Lattice Vibrations of Manganese Oxides: Part I. Periodic Structures. *Spectrochim. Acta, Part A* **2004**, *60*, 689−700.
(41) Salimi, A.; Mamkhezri, H.; Hallaj, R.; Soltanian, S. Electrochemical Detection of Trace Amount of Arsenic(III) at Glassy Carbon Electrode Modified with Cobalt Oxide Nanoparticles. *Sens. Actuators B Chem* **2008**, *129*, 246−254.


DOI: 10.1021/acsami.9b06023
*ACS Appl. Mater. Interfaces* 2019, 11, 28154−28163